DNA-PKcs phosphorylation at the T2609 cluster alters the repair pathway choice during immunoglobulin class switch recombination

Jennifer L. Crowe[a,b,1], Xiaobin S. Wang[a,b,1], Zhengping Shao[a], Brian J. Lee[a], Verna M. Estes[a], and Shan Zha[a,c,2]

[a]Institute for Cancer Genetics, Vagelos College of Physicians and Surgeons, Columbia University, New York, NY 10032; [b]Graduate Program of Pathobiology and Molecular Medicine, Vagelos College of Physicians and Surgeons, Columbia University, New York, NY 10032; and [c]Division of Pediatric Oncology, Hematology and Stem Cell Transplantation, Department of Pediatrics, Vagelos College of Physicians & Surgeons, Columbia University, New York, NY 10032

Edited by John Tainer, Departments of Cancer Biology and of Molecular and Cellular Oncology, The University of Texas M.D. Anderson Cancer Center, Houston, TX, and accepted by Editorial Board Member Philip C. Hanawalt August 7, 2020 (received for review April 18, 2020)

The DNA-dependent protein kinase (DNA-PK), which is composed of the KU heterodimer and the large catalytic subunit (DNA-PKcs), is a classical nonhomologous end-joining (cNHEJ) factor. Naïve B cells undergo class switch recombination (CSR) to generate antibodies with different isotypes by joining two DNA double-strand breaks at different switching regions via the cNHEJ pathway. DNA-PK and the cNHEJ pathway play important roles in the DNA repair phase of CSR. To initiate cNHEJ, KU binds to DNA ends and recruits and activates DNA-PK. Activated DNA-PK phosphorylates DNA-PKcs at the S2056 and T2609 clusters. Loss of T2609 cluster phosphorylation increases radiation sensitivity but whether T2609 phosphorylation has a role in physiological DNA repair remains elusive. Using the *DNA-PKcs*^{5A} mouse model carrying alanine substitutions at the T2609 cluster, here we show that loss of T2609 phosphorylation of DNA-PKcs does not affect the CSR efficiency. Yet, the CSR junctions recovered from *DNA-PKcs*$^{5A/5A}$ B cells reveal increased chromosomal translocations, extensive use of distal switch regions (consistent with end resection), and preferential usage of microhomology—all signs of the alternative end-joining pathway. Thus, these results uncover a role of DNA-PKcs T2609 phosphorylation in promoting cNHEJ repair pathway choice during CSR.

class switch recombination | nonhomologous end joining | alternative end joining | DNA-PKcs | T2609 autophosphorylation

DNA-dependent protein kinase (DNA-PK), which is composed of the KU70 and KU86 (Ku80 in mouse) heterodimer (KU) and the large catalytic subunit (DNA-PKcs), is a member of the classical nonhomologous end-joining (cNHEJ) pathway. As a major DNA double-strand break (DSB) repair pathway in mammalian cells, cNHEJ entails both end processing and end ligation. KU initiates cNHEJ by binding to the double-stranded DNA (dsDNA) ends, which, in turn, recruits and activates DNA-PKcs that, among other functions, activates the Artemis endonuclease for end processing (1, 2). KU also interacts with and stabilizes the LIG4/XRCC4/XLF complex for end ligation. In animal models, loss of cNHEJ-mediated end ligation (e.g., *Lig4*$^{-/-}$) leads to severe neuronal apoptosis, which causes embryonic lethality in the case of *Xrcc4*$^{-/-}$ and *Lig4*$^{-/-}$ mice (3). In contrast, loss of DNA-PKcs or Artemis increases radiation sensitivity but does not cause measurable neuronal apoptosis, consistent with their relatively limited roles in direct end ligation (4–6). Several new cNHEJ factors (e.g., PAXX and CYREN/MRI) are characterized based on their interaction with KU. Loss of PAXX or CYREN/MRI increases radiation sensitivity but only abrogates end ligation if XLF, a nonessential cNHEJ factor, is also lost simultaneously (7–11).

In addition to general DSB repair, developing lymphocytes undergo programmed DSB and repair events to assemble and modify the immunoglobulin heavy chain (IgH) genes. Specifically, V(D)J recombination, which occurs in progenitor lymphocytes, assembles the variable region exon from individual V, D, and J gene segments exclusively via cNHEJ. DNA-PKcs and Artemis are required for opening the hairpin at the coding ends during V(D)J recombination. Correspondingly, *DNA-PKcs*$^{-/-}$ (null) or *Artemis*$^{-/-}$ mice are born of normal size at the expected ratio but develop severe combined immunodeficiency (SCID) (4–6). Patients with hypomorphic mutations in DNA-PKcs or Artemis also develop SCID (12, 13). Mature B cells also undergo class switch recombination (CSR), which replace the initially expressed IgM constant region with another downstream constant region encoding a different isotype, to generate antibodies with different effector functions. The cNHEJ pathway plays an important role in CSR. However, in cells lacking a core cNHEJ factor (e.g., Lig4 or Xrcc4), up to 25–50% of CSR can be achieved by the alternative end-joining (Alt-EJ) pathway that preferentially uses microhomology (MH) at the junctions (14–16). Consistent with DNA-PKcs and Artemis being dispensable for direct end ligation, *DNA-PKcs*$^{-/-}$ B cells only have moderate defects in CSR (17, 18). Nevertheless, in recent high-throughput sequence analyses, we found that CSR junctions recovered from *DNA-PKcs*$^{-/-}$ B cells contained increased chromosomal translocations and extensive end resection, and preferentially used MHs (19), suggesting that the seemingly robust CSR achieved in *DNA-PKcs*$^{-/-}$ cells is primarily mediated by the Alt-EJ pathway like those in *Lig4*$^{-/-}$

Significance

DNA-dependent protein kinase (DNA-PK), which is composed of the KU heterodimer and the large catalytic subunit (DNA-PKcs), is a classical nonhomologous end-joining (cNHEJ) factor with important roles in immunoglobulin class switch recombination. Activated DNA-PK phosphorylates many substrates, including DNA-PKcs itself at the T2609 cluster. Using knockin mouse models, we found that while the loss of T2609 phosphorylation of DNA-PKcs does not affect class switch recombination (CSR) efficiency, the CSR junctions recovered from T2609A B cells are generated by the alternative end-joining pathway, providing the evidence for a role of DNA-PKcs T2609 phosphorylation in DNA repair pathway choice.

Author contributions: J.L.C., X.S.W., and S.Z. designed research; J.L.C., X.S.W., B.J.L., V.M.E., and S.Z. performed research; J.L.C., X.S.W., Z.S., and S.Z. contributed new reagents/analytic tools; J.L.C., X.S.W., B.J.L., and S.Z. analyzed data; and J.L.C., X.S.W., and S.Z. wrote the paper.

The authors declare no competing interest.

This article is a PNAS Direct Submission. J.T. is a guest editor invited by the Editorial Board.

Published under the PNAS license.

[1]J.L.C. and X.S.W. contributed equally to this work.

[2]To whom correspondence may be addressed. Email: sz2296@columbia.edu.

This article contains supporting information online at https://www.pnas.org/lookup/suppl/doi:10.1073/pnas.2007455117/-/DCSupplemental.

First published August 31, 2020.

Downloaded at Palestinian Territory, occupied on December 11, 2021

www.manaraa.com

or *Xrcc4*$^{-/-}$ B cells (14, 15). Accordingly, human patients with spontaneous mutations in DNA-PKcs also show severe defects in both V(D)J recombination and CSR and increased MH in the residual CSR junctions (12, 20).

DNA-PKcs is the best-characterized substrate of DNA-PK (21). In a previous study, we showed that mice carrying a knockin kinase-dead mutation of DNA-PKcs (*DNA-PKcs*^{KD}) die in utero with severe neuronal apoptosis, like *Lig4*$^{-/-}$ or *Xrcc4*$^{-/-}$ mice (22). KU deletion rescued the embryonic development of *DNA-PKcs*$^{KD/KD}$ mice, suggesting that DNA-PKcs has an end-capping function at the DNA ends that is regulated by its kinase activity (22). Correspondingly, *DNA-PKcs*$^{KD/KD}$ mature B cells display severe CSR defects like *Lig4*$^{-/-}$ B cells, and the residual CSR junctions from *DNA-PKcs*$^{KD/KD}$ B cells are all mediated by the Alt-EJ pathway (19)

Three DNA damage-induced phosphorylation clusters on DNA-PKcs have been characterized: the S2056 cluster, the T2609 cluster, and the S3590 cluster (Fig. 1*A*) (23–26). Among them, the T2609 cluster can also be cross-phosphorylated by ATM upon ionizing radiation (27, 28) and by ATR upon ultraviolet (UV) radiation (29). Human DNA-PKcs with alanine substitutions at the S2056 cluster and/or the T2609 cluster cannot restore radiation resistance in DNA-PKcs–deficient Chinese hamster ovary (CHO) cells (24, 30–33), suggesting a role of DNA-PKcs phosphorylation in DSB repair. The mouse model carrying alanine substitutions in the S2056 cluster (*DNA-PKcs*$^{PQR/PQR}$) has no defect in chromosomal V(D)J recombination or CSR, despite moderate radiation sensitivity (34). Mouse models with alanine substitutions of three or all five threonine residues at the T2609 cluster (*DNA-PKcs*$^{3A/3A}$ or *DNA-PKcs*$^{5A/5A}$) succumb to neonatal bone marrow failure that abolishes both myeloid and lymphoid progenitors (35–37). *Tp53* deficiency restores lymphocyte development and peripheral mature lymphocyte counts in *DNA-PKcs*$^{3A/3A}$ and *DNA-PKcs*$^{5A/5A}$ mice. The v-abl kinase transformed *DNA-PKcs*$^{3A/3A}$ and *DNA-PKcs*$^{5A/5A}$ B cells undergo robust chromosomal V(D)J recombination in culture (37, 38), suggesting that T2609 phosphorylation is not required for V(D)J recombination.

Here, we analyzed the impact of DNA-PKcs T2609 phosphorylation on CSR in mature B cells isolated from *DNA-PKcs*$^{5A/5A}$ mice carrying *Tp53* deficiency (heterozygous or homozygous). While CSR efficiency is not affected by alanine substitution at the T2609 cluster, high-throughput genomic translocation sequence (HTGTS) analyses reveal that the CSR junctions from *DNA-PKcs*$^{5A/5A}$ B cells contain increased chromosomal translocations, extensive use of downstream switch regions (consistent with end resection), and increased MHs—all signatures of the Alt-EJ pathway, suggesting a role of DNA-PKcs T2609 phosphorylation in repair pathway choice during CSR.

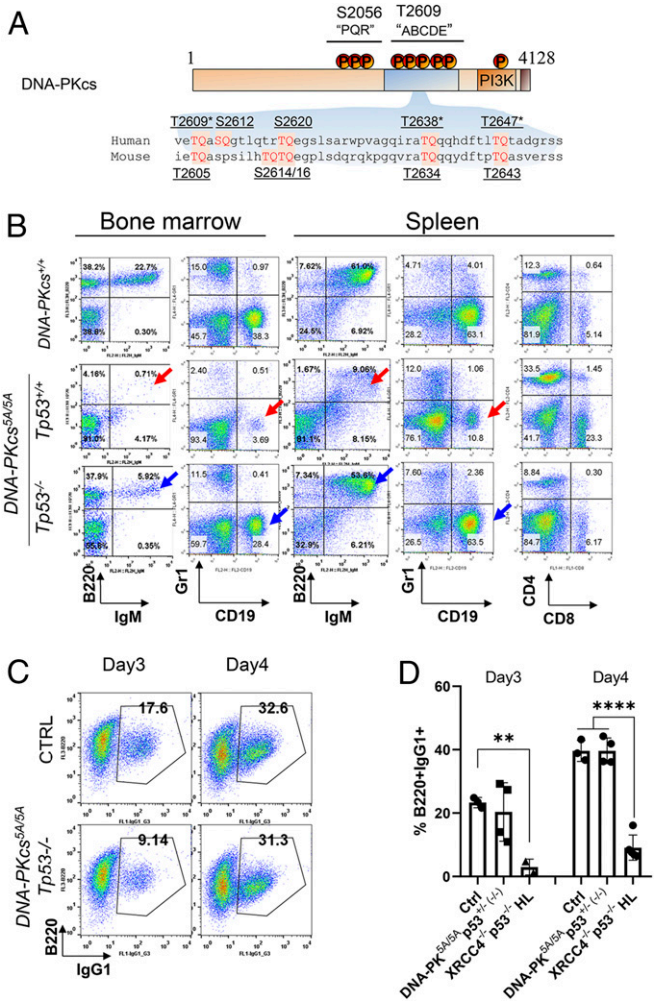

Fig. 1. Class switch recombination is transiently delayed in *DNA-PKcs*$^{5A/5A}$ cells. (*A*) Diagram of the DNA-PKcs protein and the organization of the T2609 cluster on human DNA-PKcs and the corresponding T2605 cluster on mouse DNA-PKcs. The conserved T2609, T2636, and T2647 are marked with asterisks. The *DNA-PKcs*^{5A} allele contains alanine substitutions of all five threonine residues, while the previously published DNA-PKcs 3A allele contains alanine substitutions at three conserved threonine residues. (*B*) Representative flow cytometry analyses of B and T cell development in *DNA-PKcs*$^{5A/5A}$ and *DNA-PKcs*$^{5A/5A}$*Tp53*$^{-/-}$ mice, indicating *Tp53* deficiency restored peripheral mature B cells (IgM+B220+) in *DNA-PKcs*$^{5A/5A}$ mice. (*C*) Representative flow cytometry analyses of class switch recombination to IgG1 at day 3 and day 4 after cytokine activation. (*D*) Quantification of IgG1 switching. The bars mark the SEs. There is no significant difference between *DNA-PKcs*$^{5A/5A}$ and *DNA-PKcs*$^{+/+}$ B cells. $^{**}P < 0.01$, $^{****}P < 0.0001$, unpaired Student's *t* test, between *DNA-PKcs*$^{+/+}$ and *XRCC4*$^{-/-}$*HL*$^{k/k}$ cells.

Materials and Methods

Generation and Characterization of the Mouse Models. *Xrcc4*$^{-/-}$, *DNA-PKcs*$^{-/-}$, *p53*$^{-/-}$, and the prearranged IgH heavy and light chain knock-in alleles (HL$^{k/k}$) that bypass the need for DNA-PKcs in early B cell development have been described previously (4, 39–42). The *DNA-PKcs*^{5A} allele and the generation of the *DNA-PKcs*$^{5A/5A}$ mouse model were recently published (37). The *DNA-PKcs*^{5A} mutation converts all five threonine residues in the T2605 cluster (T2609 in human) encoded by exon 58 of murine *DNA-PKcs* to alanine residues (Fig. 1*A*). Briefly, DNA sequences (5′ and 3′ arms) from the genomic DNA-PKcs (*Prkdc*) locus were isolated via polymerase chain reaction (PCR) and cloned into the pGEMT vector. We synthesized an ∼500-bp fragment containing all of the mutations (Genewiz), inserted it into an extended 3′ arm (4.4 kb) in pGEMT. The correct sequence was confirmed by Sanger sequencing. The 5′ arm and the extended 3′arm with the mutations were then inserted into the pEMCneo vector that carries a Neo-Resistance (NeoR) gene flanked by a pair of FRT sites. The Sma1-linearized plasmids were electroporated into murine embryonic stem cells (129Sv background), and NeoR^{+} clones were isolated and screened by Southern blotting and Sanger sequencing (Fig. 1*A*) (37). Upon injection and germ-line transmission, the resultant *DNA-PKcs*$^{+/5AN}$ mice (N for NeoR containing) were crossed with mice expressing FLIP recombinase constitutively, *Rosa26a*$^{FLIP/FLIP}$ (Jax stock no. 003946, also in 129Sv background), to remove the NeoR cassette and allow the expression of the DNA-PKcs-5A protein. All animal work was conducted in a specific pathogen-free facility, and all of the procedures were approved by the Institutional Animal Care and Use Committee at Columbia University Medical Center.

Lymphocyte Development Analyses. Single-cell suspensions were prepared from the thymus, bone marrow, and spleen of young adult (6–8 wk) mice. Splenocytes were treated with red blood cell lysis buffer (Lonza ACK Lysis Buffer) for 1–2 min at room temperature to remove mature erythrocytes. Approximately 1 × 10^{5} cells were stained using fluorescence-conjugated antibodies and analyzed by flow cytometry (11, 22). The following antibody mixtures were used for B cell (FITC anti-mouse CD43, BioLegend, 553270; PE Goat anti-mouse IgM, Southern Biotech, 1020-09; PE-Cyanine5 anti-Hu/Mo CD45R (B220), eBioScience, 15-0452-83; and APC anti-mouse

Downloaded at Palestinian Territory, occupied on December 11, 2021
www.manaraa.com

TER119, BioLegend, 116212) and T cell (PE rat anti-mouse CD4, BioLegend, 557308; FITC anti-mouse CD8a, BioLegend, 100706; PE/Cy5 anti-mouse CD3e, eBioscience, 15-0031-83; and APC anti-mouse TCRβ, BD Pharmingen, 553174) analyses. The dead cells and debris were excluded based on their high side scatter and low forward scatter. Since the bone marrow and spleen contain a variable number of erythrocytes after red blood cell lysis, we used the Ter119 (an erythrocyte marker) antibody to gate out the red blood cells before the analyses of B, T, and myeloid cell-specific markers as in Fig. 1.

Class Switch Recombination Analyses. For the CSR assay, $CD43^-$ splenocytes were isolated with magnetic beads (MACS, Miltenyi Biotec) and cultured ($5–10 \times 10^5$ cells·mL^{-1}) in RPMI (GIBCO) supplemented with 15% fetal bovine serum (FBS) (HyClone) and 2 μg·mL^{-1} anti-CD40 (BD Bioscience) plus 20 ng·mL^{-1} IL-4 (R&D). Cells were maintained daily at 1×10^6 cells·mL^{-1} and collected for flow cytometry analyses after staining for IgG1 and B220 (FITC anti-IgG1, BD Pharmingen, and PE Cy5 anti-B220, eBioscience). Flow cytometry data were collected on a FACSCalibur flow cytometer (BD Bioscience) and processed using the FlowJo V10 software package. For the Cell Trace Violet (CTV) staining, purified B cells were incubated at 6×10^6 cells·mL^{-1} in 1 mL of PBS with 1 μL of 5 mM CTV dye (Thermo Scientific). The CTV-stained B cells were washed and activated as detailed above and subjected to flow cytometry analyses 4 d after activation.

HTGTS of CSR Junctions. HTGTS was performed as previously described (19, 43). Briefly, genomic DNA was collected from activated B cells 4 d after stimulation, sonicated (Diagenode Bioruptor), and amplified with an Sμ specific biotinylated primer (5′/5BiosG/CAGACCTGGGAATGTATGGT3′) and nested primer (5′CACACAAAGACTCTGGACCTC3′). AflII was used to remove germ-line (nonrearranged) sequences. Since all mice were of pure 129 background, the IgH switch region (from JH4 to the last Cα exon, chr12: 114,494,415–114,666,816) of the C57/BL6 based mm9 genome was replaced with the corresponding region of the AJ851868.3 129 IgH sequence (1415966–1592715) to generate the mm9sr (switch region replacement) genome, and the sequencing analyses were performed as detailed previously (43, 44). The best-path searching algorithm (related to YAHA; ref. 45) was used to identify optimal sequence alignments from Bowtie2-reported top alignments (alignment score > 50). The reads were filtered to exclude mispriming, germ-line (unmodified), sequential joints, and duplications. To plot all of the S-region junctions, including those within the repeats and, thus, have low mappability but unequivocally mapped to an individual switch region, we combined the ones filtered by a mappability filter but unequivocally mapped to S regions with "good" reads passing both the mappability filters (both deduplicated) (43). MHs are defined as regions of 100% homology between the bait and prey-break sites. Insertions are defined as regions containing nucleotides that map to neither the bait nor prey-break site. Blunt junctions are considered to have no MHs or insertions. We calculated the AGCT or RGYW motif frequency in each switch region using the IgH region sequence from the 129/Sv strain (accession no. AJ851868.3). The mutation rate was calculated by a customized Excel integrated VBA script. Specifically, we analyzed the mutations in the bait portion by comparing the actual bait sequence of each IgH junction with the germ-line bait sequence from the 129/Sv strain (accession no. AJ851868.3). Only true mismatches (no insertion or deletion) were counted as mutations. The HTGTS data reported in this paper have been deposited in the Gene Expression Omnibus (GEO) database, https://www.ncbi.nlm.nih.gov/geo/ (accession nos. GSE117628 and GSE154210).

Western Blotting. The B cells were lysed with a buffer containing 50 mM Tris·Cl (pH 7.3), 137 mM NaCl, 10% Glycerol, 1% Triton X-100, 0.2% Sarkosyl, and freshly added NaF (10 mM), phenylmethylsulfonyl fluoride (PMSF) (1 mM), 1× protease inhibitor mixture (Sigma), and benzonase (0.625 U/μL) to generate whole-cell lysate. Western blot analysis was performed using the standard protocol and blotted with the following primary antibodies: anti-total ATM (Sigma A1106-200UL 1:1,000), pATM S1981(S1987 mouse) (Cell Signaling 4526S), pKAP1 S824 (1:1,000, A300-767A, Bethyl Laboratories), pH2AX Ser139 (1:1,000, 07-164, Millipore), total H2AX (1:1,000, 07-627, Millipore), vinculin (1:1,000, V284, 05-386 Millipore). Horeradish peroxidase (HRP)-conjugated anti-rabbit and mouse secondary antibodies (GE Healthcare) were used and an enhanced chemiluminescence (ECL) Western blotting detection system (GE Healthcare) was used for detection.

Results

Loss of the Tp53 Tumor Suppressor Gene Restores Peripheral B Cells in *DNA-PKcs$^{5A/5A}$* Mice. The human DNA-PKcs T2609 phosphorylation cluster contains five TQ sites, among which, T2609, T2638, and T2647 (T2605, T2634, and T2643 in mouse, respectively) are conserved (Fig. 1*A*) (21, 31, 32). To investigate the impact of the DNA-PKcs T2609 cluster of phosphorylation, we replaced all five threonine residues in this region with alanines and named the allele -5A. Similar to the previously published 3A allele (which replaces the three conserved threonines) (35), the *DNA-PKcs$^{5A/5A}$* mice were born alive with hyperpigmented toes but succumbed to bone marrow failure by 3 wk with very few mature lymphocytes (37) (Fig. 1*B* and *SI Appendix*, Fig. S1 *A* and *B*). *Tp53* deficiency, both heterozygous and homozygous, rescues the growth retardation, corrects the hyperpigmentation, and, most importantly, restores peripheral splenic B cell frequency (Fig. 1*B* and *SI Appendix*, Fig. S1 *A* and *B*), consistent with the dispensable role of T2609 phosphorylation in V(D)J recombination (37, 38).

***DNA-PKcs$^{5A/5A}$* B Cells Undergo Slightly Delayed, but Efficient Class Switch Recombination.** To understand the role of DNA-PKcs T2609 phosphorylation in CSR, we purified splenic B cells from *DNA-PKcs$^{5A/5A}$Tp53$^{+/-(or\ -/-)}$* and control *DNA-PKcs$^{+/+}$* or *Tp53$^{+/-(or\ -/-)}$* mice and cultured them with anti-CD40 and interleukin 4 (IL-4) that induce robust CSR to IgG1 and IgE. *Tp53* deficiency does not affect CSR efficiency or CSR junctions (15, 19, 46, 47). About 20% of *DNA-PKcs$^{+/+}$* B cells were IgG1+ after 3 d of stimulation and ∼37% IgG1+ by day 4 (Fig. 1 *C* and *D*). In comparison, *DNA-PKcs$^{5A/5A}$Tp53$^{+/-(or\ -/-)}$* B cells achieved ∼15% $IgG1^+$ B cells by day 3 and eventually 30–40% $IgG1^+$ by day 4 of activation (Fig. 1 *C* and *D*). Successful CSR requires cell proliferation. Cell division analyses via the CTV dye did not find proliferation defects in *DNA-PKcs$^{5A/5A}$Tp53$^{+/-(or\ -/-)}$* B cells (*SI Appendix*, Fig. S1*C*), consistent with the largely normal weight and peripheral lymphocyte numbers of *DNA-PKcs$^{5A/5A}$Tp53$^{+/-(or\ -/-)}$* mice (*SI Appendix*, Fig. S1*A*) (37). As a control, naive B cells lacking Xrcc4, the obligatory partner of Lig4, were generated from mice carrying productive IgH/Igκ arrangements as well as Tp53 deficiency to overcome V(D)J recombination defects and embryonic lethality, respectively. Upon activation, *Xrcc4$^{-/-}$* B cells achieved 5% of IgG1+ on day 3 and ∼10% on day 4, ($P = 0.0014$, and $P < 0.0001$, respectively) (Fig. 1*D*), consistent with the 25–50% residual CSR in Xrcc4- or Lig4-deficient cells documented before (14–16). Under similar conditions, *DNA-PKcs$^{-/-}$* cells achieve 80–90% of IgG1 CSR (18, 19, 48). These data suggest that phosphorylation of DNA-PKcs at the T2609 cluster is dispensable for efficient CSR, in contrast to the loss of Xrcc4 or DNA-PKcs.

T2609 Cluster Phosphorylation Alters the Distribution of the IgH Junctions. Given *DNA-PKcs$^{-/-}$* B cells undergo nearly 90% of CSR to IgG1 via the Alt-EJ–mediated repair pathway, as detected by the HTGTS of Sμ-Sμ internal deletions and Sμ-Sγ1 CSR junctions (19), we analyzed the CSR junctions in *DNA-PKcs$^{5A/5A}$p53$^{+/-(or\ -/-)}$* B cells using the sensitive HTGTS. Briefly, "translocation junctions" from a single bait site at the 5′Sμ to various targets were isolated after linear amplification and sequenced (Fig. 2*A*) (19, 43). Altogether, we analyzed 4,545 junctions from B cells derived from five different *DNA-PKcs$^{5A/5A}$p53$^{+/-(or\ -/-)}$* mice and over 10,000 junctions total from control *DNA-PKcs$^{+/+}$*, *Tp53$^{+/-}$*, *DNA-PKcs$^{-/-}$*, and *Xrcc4$^{-/-}$* B cells. As shown in Fig. 2*B*, nearly 90% of all junctions isolated from *DNA-PKcs$^{+/+}$*, *Tp53$^{-/-}$* or *Tp53$^{+/-}$*, *DNA-PKcs$^{5A/5A}$p53$^{+/-(or\ -/-)}$*, and *DNA-PKcs$^{-/-}$* mature B cells are joined with a target (referred as "Prey") within the IgH locus (defined as a 400-kb region including all D, J elements, and Constant regions). We further defined the orientation of Prey junctions as (+) if it reads from centromere to telomere after the junction, or as (-) if it reads from telomere to

Downloaded at Palestinian Territory, occupied on December 11, 2021

www.manaraa.com

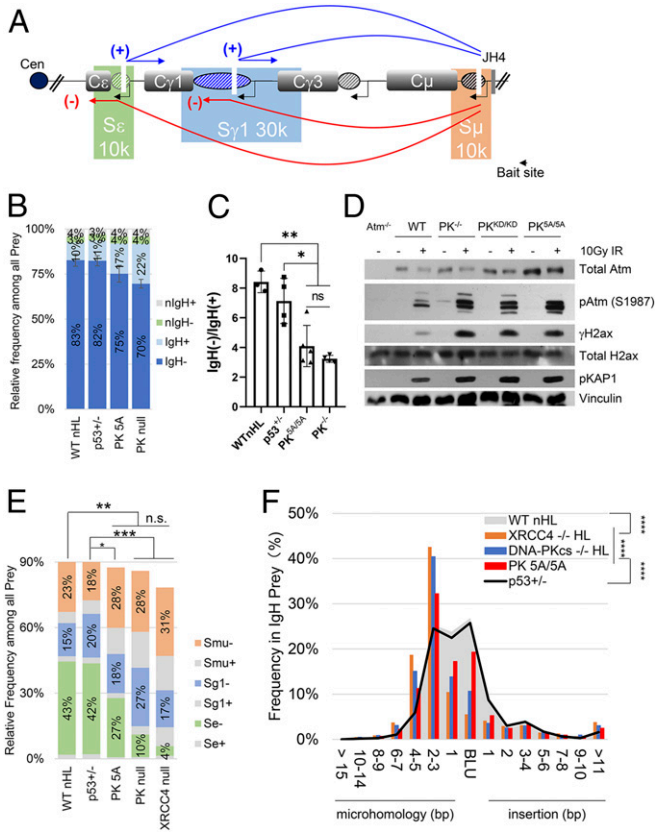

Fig. 2. Class switch recombination in *DNA-PKcs*$^{5A/5A}$ cells have increased MH. (*A*) Diagram of the murine IgH locus with the location of Sμ (beige), Sγ1 (blue), and Sε (green). The bait site is marked on the lower right of the diagram. The red (deletional, (-) strand) and blue (inversional, (+) strand) arrows indicate the orientation of potential junctions. (*B*) Relative frequency of HTGTS junctions in the (-) and (+) strand orientation, and in the IgH or non-IgH regions. The *y* axis shows the relative frequency among all preys. We defined the junction as (+) orientation if the reads are aligned from the centromere to the telomere, and as (-) if the reads are aligned from the telomere to the centromere. The IgH region is defined as 400 kb including part of V, all D, all J segments, and the entire switch region. This graph focuses on the relative frequency of IgH preys and the orientation of the preys. The error bars represent SDs. (*C*) Ratio between the total number of junctions mapped to (-) strand of IgH and (+) strand of IgH; the $^{**}P < 0.01$, $^{*}P < 0.05$, n.s. (not significant) for unpaired Student's *t* test between the IgH (-) prey%. (*D*) Western blotting of ATM protein levels and radiation (10 Gy) induced Atm autophosphorylation (S1987) and Kap1 and H2AX phosphorylation in B cells of corresponding genotypes. The lysates were collected 2 h after ionizing radiation. (*E*) Frequency of HTGTS junctions in the (-) and (+) strand orientation, and in the IgH regions, subdivided into Sμ, Sγ1, and Sε. The *y* axis shows the relative frequency among all preys. This figure highlights the distribution of the IgH preys among different switch regions. The data represents the pool of five *DNA-PKcs*$^{5A/5A}$ mice, three *DNA-PKcs*$^{+/+}$ mice (WT), four *DNA-PKcs*$^{-/-}$, and a total of four (two each) *Tp53*$^{-/-}$ or *Tp53*$^{+/-}$ mice. $^{**}P < 0.01$ (n.s, not significant) for unpaired Student's *t* test. (*F*) Frequency of junctions with MHs, Blunt (BLU), and insertions (INS). $^{****}P < 0.0001$ (n.s., not significant) for the Kolmogorov–Smirnov test.

centromere. Since the IgH locus resides on the (-) strand of murine chromosome 12 and the bait at the 5′ Sμ reads from telomere to centromere, the normal internal deletion (Sμ-Sμ) and class switch recombination (Sμ-Sγ1, or Sμ-Sε) junctions are in the (-) orientation (Fig. 2*A*). Indeed, >80% of all preys from *DNA-PKcs*$^{+/+}$ (WT) and *Tp53*-deficient B cells fall on the (-) strand of IgH (83% for WT and 82% for *Tp53*-deficient). Only 10% of all preys from *DNA-PKcs*$^{+/+}$ (WT) and 11% of those from *Tp53*-deficient cells fall on the (+) strands of IgH (Fig. 2 *A* and *B*). In contrast, 75% of all preys from *DNA-PKcs*$^{5A/5A}$ B cells are on the IgH (-) strand and 17% on the IgH (+) strand, similar to those in control *DNA-PKcs*$^{-/-}$ B cells (70% IgH- and 22% IgH+) (Fig. 2*B*) (19). As a result, the IgH (-) vs. IgH (+) ratio is significantly lower in preys recovered from *DNA-PKcs*$^{5A/5A}$ (average 4.48) and *DNA-PKcs*$^{-/-}$ B cells (average 3.14) in comparison to 8.40 in *DNA-PKcs*$^{+/+}$ (WT) and 7.27 in *Tp53*-deficient cells (Fig. 2*C*). To understand the significance of the relative increases of the IgH+ preys among all IgH preys, we examined the orientation of the interchromosomal preys outside of the IgH locus (which were almost entirely to another chromosome beyond chromosome 12). Non-IgH (nIgH) preys fall equally on (+) and (-) strands in all genotypes tested (Fig. 2*B*), suggesting that the negative strand bias among the IgH preys reflects a strong preference for intrachromosomal deletion joining. Thus, we hypothesized that the relative increase of IgH preys falling on the (+) strand in *DNA-PKcs*$^{5A/5A}$ and *DNA-PKcs*$^{-/-}$ B cells reflects either increased inversional events (as illustrated with blue arrows in Fig. 2*A*) or increased intersister chromatid or interchromosomal translocations (between IgH of two homologous chromosomes 12). A similar phenotype has been noted for B cells lacking cNHEJ factors (e.g., *Xrcc4*$^{-/-}$) or DNA damage response factors (e.g., *Atm*$^{-/-}$ and *Tpr53BP1*$^{-/-}$) (19, 49–52). We note that ATM protein levels or ATM kinase activity measured by radiation-induced autophosphorylation of Atm (serine 1987 of mouse Atm) and its substrates Kap1 and H2AX were not compromised in *DNA-PKcs*$^{5A/5A}$ and *DNA-PKcs*$^{-/-}$ B cells (Fig. 2*D*), indicating that the increase in chromosomal translocations or inversion in *DNA-PKcs*$^{5A/5A}$ cells cannot be explained by compromised of ATM kinase activity.

The cytokine combination anti-CD40 and IL-4 induce CSR to IgG1 and IgE. Accordingly, ~42% of all junctions from *DNA-PKcs*$^{+/+}$, and *Tp53*$^{-/-}$ or *Tp53*$^{+/-}$ mice were located in Sε (-) (potentially IgE switching), 15~20% in Sγ1(-) (potentially IgG1 switching), and 18–23% in Sμ (-) (internal deletion) (Fig. 2*E*). IgH junctions from both *DNA-PKcs*$^{-/-}$ and *DNA-PKcs*$^{5A/5A}$ B cells have a greatly increased the Sμ (-) portion (28%) with a corresponding reduction in Sε (-) preys (10% and 27%, respectively) (Fig. 2*E*). The overall proportion of changes is more dramatic in those from *DNA-PKcs*$^{-/-}$ B cells than those from *DNA-PKcs*$^{5A/5A}$ B cells (19). Together, these data suggest that despite normal CSR efficiency, the junctions from *DNA-PKcs*$^{5A/5A}$ B cells contain increased translocations (to the [+] strand) and preferential loss of Sμ-Sε junctions—both features of cNHEJ deficiency, similar to those from *DNA-PKcs*$^{-/-}$ cells (19). Correspondingly, fluorescence in situ hybridization with a telomere probe, which increases the sensitivity to IgH locus breaks near the telomere described before (53), also revealed increased genomic instability, including both chromosome breaks at both sister chromatids and chromatid breaks in activated *DNA-PKcs*$^{5A/5A}$ B cells (*SI Appendix*, Fig. S2 *A–C*).

Loss of T2609 Cluster Phosphorylation Increases MH Usage in CSR Junctions. In the absence of cNHEJ, including the loss of DNA-PKcs, significant CSR is achieved via the Alt-EJ pathway that preferentially uses MHs at the junction (14, 15, 19). In a recent analysis, we identified two features associated with Alt-EJ–dependent CSR using HTGTS (19)—increased usage of MH at the junctions and evidence of extensive resection in switch regions. Indeed, junctions from *DNA-PKcs*$^{-/-}$ B cells with only moderate CSR defects contain both features (17, 18). Among CSR junctions (including all IgH preys) recovered from *DNA-PKcs*$^{+/+}$ or *Tp53*-deficient (alone) cells, ~25% are blunt, ~25% have 1-nt MH, and another ~25% have 2- to 3-nt MH. In contrast, less than 10% of junctions from *Xrcc4*$^{-/-}$, <15% from *DNA-PKcs*$^{-/-}$, and <20% from *DNA-PKcs*$^{5A/5A}$ cells were blunt. The frequency of junctions with 1-nt MH is also significantly decreased in *DNA-PKcs*$^{5A/5A}$, although to a lesser extent than in *Xrcc4*$^{-/-}$ or *DNA-PKcs*$^{-/-}$ cells (Fig. 2*F*). A prominent 40% of

Downloaded at Palestinian Territory, occupied on December 11, 2021
www.manaraa.com

junctions from *Xrcc4*$^{-/-}$ or *DNA-PKcs*$^{-/-}$ B cells and 32% of the IgH junctions from *DNA-PKcs*$^{5A/5A}$ B cells have 2- to 3-nt MH. Indeed, cumulatively, nearly 15% of IgH junctions from *DNA-PKcs*$^{5A/5A}$ B cells and nearly 25% from *Xrcc4*$^{-/-}$ or 20% from *DNA-PKcs*$^{-/-}$ B cells have >4-nt MH (in contrast to ∼10% in *DNA-PKcs*$^{+/+}$ or *Tp53*-deficient alone) (Fig. 2*F*). The overall frequency of insertions within IgH junctions did not differ between genotypes (Fig. 2*F*). Together these findings indicate that the loss of the T2609 cluster phosphorylation of DNA-PKcs unleashed a robust MH-mediated CSR that compensates for the moderate loss of cNHEJ. Our HTGTS analyses with over 10,000 junctions also reveal that the levels of MH usage are quantitatively different: higher in *Xrcc4*$^{-/-}$ or *DNA-PKcs*$^{-/-}$ B cells than in *DNA-PKcs*$^{5A/5A}$ B cells.

Loss of Phosphorylation at the T2609 Cluster Increases the Usage of Downstream Switch Regions. Next, we mapped the junctions within and around each specific switch region. The (+) and (-) ptoriented junctions were plotted above (blue) and below (red) the centerline, respectively (Figs. 2*A* and 3–5). Since the location of the bait is fixed within the 5′ Sμ (telomeric), the majority of the Sμ joins from *DNA-PKcs*$^{+/+}$, and *Tp53*-deficient B cells are located near the bait site. The core Sμ region is defined by the sharp change of the density of the AID hotspot-AGCT motif per 50 bp (Fig. 3, *Top*). Specifically, junctions falling centromeric to Chr12:114,665,500 (mm9) were considered beyond the core Sμ. Using this standard, only ∼10% of Sμ preys recovered from *DNA-PKcs*$^{+/+}$ and *Tp53*-deficient B cells fall beyond the core Sμ region (Fig. 3). In contrast, over 15% of Sμ junctions from *DNA-PKcs*$^{5A/5A}$ B cells fall beyond the core Sμ region, while 42% fall out in *Xrcc4*$^{-/-}$ cells and ∼30% in *DNA-PKcs*$^{-/-}$ cells (Fig. 3). *DNA-PKcs*$^{5A/5A}$ junctions show a similarly wider distribution within Sγ1, with 1.66% falling downstream of Sγ1 (versus 0.14–0.54% in the controls, 2.18% in *Xrcc4*$^{-/-}$, and 2.51% in *DNA-PKcs*$^{-/-}$) (Fig. 4), and within Sε (9.13% in *DNA-PKcs*$^{5A/5A}$ junctions versus ∼6% in the controls, 29.6% in *Xrcc4*$^{-/-}$, and 15.8% in *DNA-PKcs*$^{-/-}$) (Fig. 5). Altogether, the increased usage of distal switch regions is consistent with end resection, another feature of Alt-EJ, and cNHEJ deficiency in *DNA-PKcs*$^{5A/5A}$ B cells. Again, we note that the increased usage of the downstream switch region in *DNA-PKcs*$^{5A/5A}$, although significantly higher than those in WT cells, is quantitatively less than those in *DNA-PKcs*$^{-/-}$ cells, which is less than those in *Xrcc4*$^{-/-}$ cells.

Loss of T2609 Phosphorylation Reduced G Mutations in the 5′Sμ Bait Region of IgH. Finally, we analyzed mutations in the 5′Sμ region among the junctions (Fig. 6). To compare with prior studies using Sanger sequencing, we present the data based on the top strand relative to the Sμ germ-line transcription (Fig. 6*A*). The estimated error rate for the MiSeq platform is 0.1% (10 mutations [mut]/10,000 nt). The overall mutation rate (mut/10,000 nt) and frequency of reads with mutations were both higher in IgH junctions derived from *DNA-PKcs*$^{+/+}$ and T*p53*$^{-/-}$ cells (∼27 mut/10,000 nt) than those from *DNA-PKcs*$^{5A/5A}$ cells (∼16 mut/10,000 nt) that were also Tp53 deficient (∼16 mut/10,000 nt) (Fig. 6*D*). Junctions from *DNA-PKcs*$^{-/-}$ cells also had a slightly lower mutation rate than *DNA-PKcs*$^{+/+}$ and T*p53*$^{-/-}$ cells (Fig. 6*D*). Despite a similar distribution of nucleotide types (Fig. 6*B*), G was most frequently mutated in the 5′Sμ region of *DNA-PKcs*$^{+/+}$ and *Tp53*$^{-/-}$ B cells (47 mut/10,000 G). Lower G mutation rates in *DNA-PKcs*$^{-/-}$ cells (20 mut/10,0000 G) and *DNA-PKcs*$^{5A/5A}$ cells (25 mut/10,000 G) account for a lower overall mutation rate in those cells (Fig. 6*F*). The pattern of G mutations (relative frequency to A, T, C) did not change, suggesting the reduction is likely due to AID targeting, rather than differences in secondary processing by uracil-DNA glycosylase, Mismatch repair, or other pathways (Fig. 6*C*). Moreover, there is also an overall reduction in the frequency of reads with mutations in *DNA-PKcs*$^{5A/5A}$ cells (Fig. 6*E*). Altogether, we note a reduction of G nucleotide mutations in the 5′Sμ region in *DNA-PKcs*$^{5A/5A}$ and DNA-PKcs$^{-/-}$ cells. Similar changes have been noted in cNHEJ-deficient, *Xrcc4*$^{-/-}$ and *DNA-PKcs*$^{KD/KD}$ B cells.

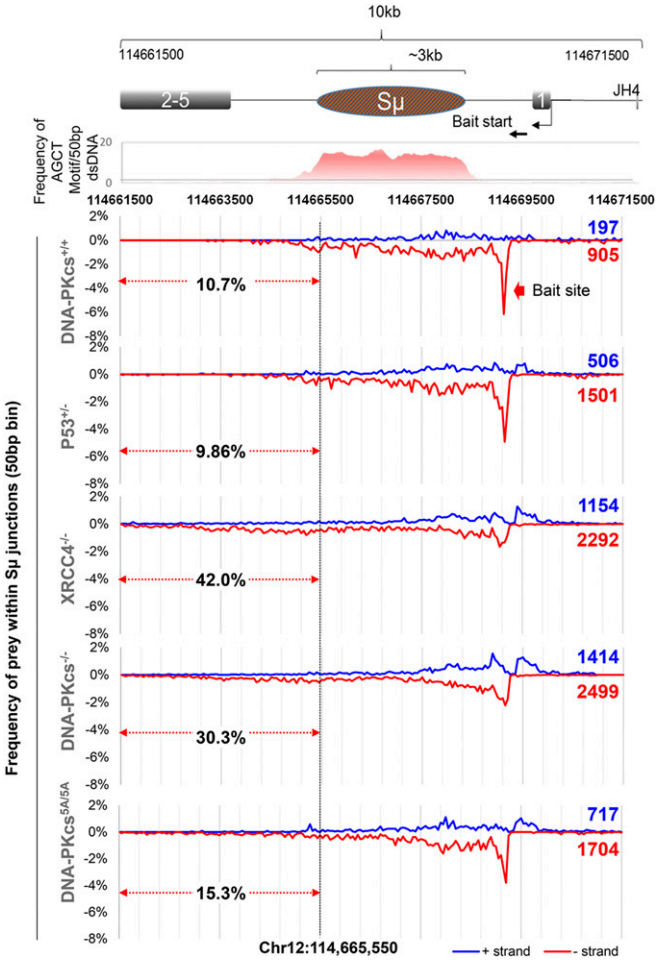

Fig. 3. Distribution of CSR junctions within 10 kb of the Sμ locus. The schematic of the region of interest is drawn at *Top*. For each genotype, the number of junctions is indicated for the (+) strand (blue) and (-) strand (red). The (-) orientation junctions are shown as negative percentages. Percent of junctional usage from the end of Sμ to the end of the 10-kb window (between chr12:114,661,500–114,665,500) is indicated with red arrows. We define the core region based on the density of the AID hotspot diagrammed above. Junctions in this range are considered resections. Bin = 50 bp. Only the percentage of negative strand junctions was used to calculate the resection %. The data represent the pool of five *DNA-PKcs*$^{5A/5A}$ mice, three *DNA-PKcs*$^{+/+}$ mice (WT), two *Xrcc4*$^{-/-}$ mice, five *DNA-PKcs*$^{-/-}$ mice, and a total of four (two each) *Tp53*$^{-/-}$ or *Tp53*$^{+/-}$ mice.

Discussion

DNA-PKcs deficiency has been linked to reduced CSR efficiency and a preference for MH in patients and mouse models (19, 20). The T2609 phosphorylation cluster is one of the most prominent posttranslational modifications of DNA-PKcs and has been associated with increased radiation sensitivity (24, 30–33), while its role in CSR remains elusive. In this context, T2609 phosphorylation has been implicated in telomere biology (36) and ribosomal biogenesis (37), which both could indirectly contribute to

Downloaded at Palestinian Territory, occupied on December 11, 2021

www.manaraa.com

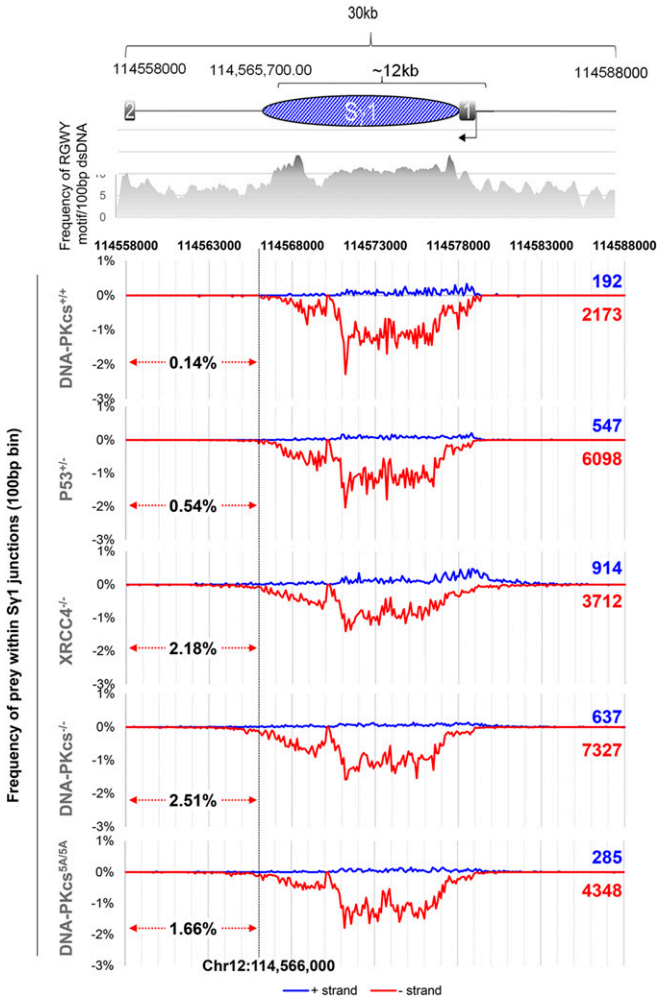

Fig. 4. Distribution of CSR junctions within 30 kb of the Sγ1 locus. The scheme of the region of interest is drawn at *Top*. For each genotype, the number of junctions is indicated for the (+) orientation (blue) and (-) orientation (red). The (-) orientation junctions are shown as negative percentages. Percent of junctional usage from the end of Sγ1 to the end of the 30-kb window (between chr12: 114558000–11456600) is indicated with red arrows (bin = 100 bp). We define the core region based on the density of the AID hotspot diagrammed above. Junctions in this range are considered resections. Only the percentage of negative-strand junctions was used to calculate the resection %. The data represent the pool of five *DNA-PKcs*$^{5A/5A}$ mice, three *DNA-PKcs*$^{+/+}$ mice (WT), two *Xrcc4*$^{-/-}$ mice, five *DNA-PKcs*$^{-/-}$ mice, and a total of four (two each) *Tp53*$^{-/-}$ or *Tp53*$^{+/-}$ mice.

radiation sensitivity. To understand the role of T2609 phosphorylation in CSR and DSB repair specifically, we evaluated the role of T2609 phosphorylation in physiological DSB repair during CSR using germ-line mouse models. As in the case of V(D)J recombination (35, 37, 38), T2609A mutation also does not affect CSR efficiency. However, CSR junctions from *DNA-PKcs*$^{5A/5A}$ B cells revealed a preferential loss of Sμ-Sε junctions, increased MH usage, increased use of downstream switch regions (consistent with excessive end resection), and increased interchromosomal translocations ([+] strand preys)—all consistent with cNHEJ deficiency and compensatory Alt-EJ–mediated CSR. Together these findings support the role of DNA-PKcs T2609 phosphorylation in promoting cNHEJ-mediated CSR. In the absence of T2609 phosphorylation, the increased dependence on the Alt-EJ pathway, together with the extensive length of the Sγ1 region (12.5 kb in 129SV strain), the dense RGYW/AGCT sequence motifs (Fig. 4), and the sequence-independent 3D interactions (synapses) between Sμ-Sγ1 (54–57), lead to robust Alt-EJ–mediated CSR to IgG1 in *DNA-PKcs*$^{5A/5A}$ B cells. Thus, our analyses identify a role of DNA-PKcs T2609 phosphorylation in repair pathway choice during CSR.

The estimated error rate of the Illumina Miseq platform is 0.1%, which is lower than the estimated and reported somatic hypermutation (SHM) rate (58) and, therefore, allows for analyses of SHM. As previously reported (59, 60), G mutations are two times more frequent than C mutations on the top strand of the 5′Sμ region (the nontemplate strand relative to Sμ germ-line transcription). Interestingly, the T2609A mutation attenuated this preference of G mutations, while the pattern of G mutations (relative to A, C, T) is unaffected, suggesting that the T2609A mutation and its associated repair defects might compromise AID targeting to 5′Sμ without affecting U:G mismatch processing. Consistent with this model, the frequency of reads with mutations also decreased in *DNA-PKcs*$^{5A/5A}$ B cells. The bias of APOBEC family enzymes to deaminate the lagging strand during

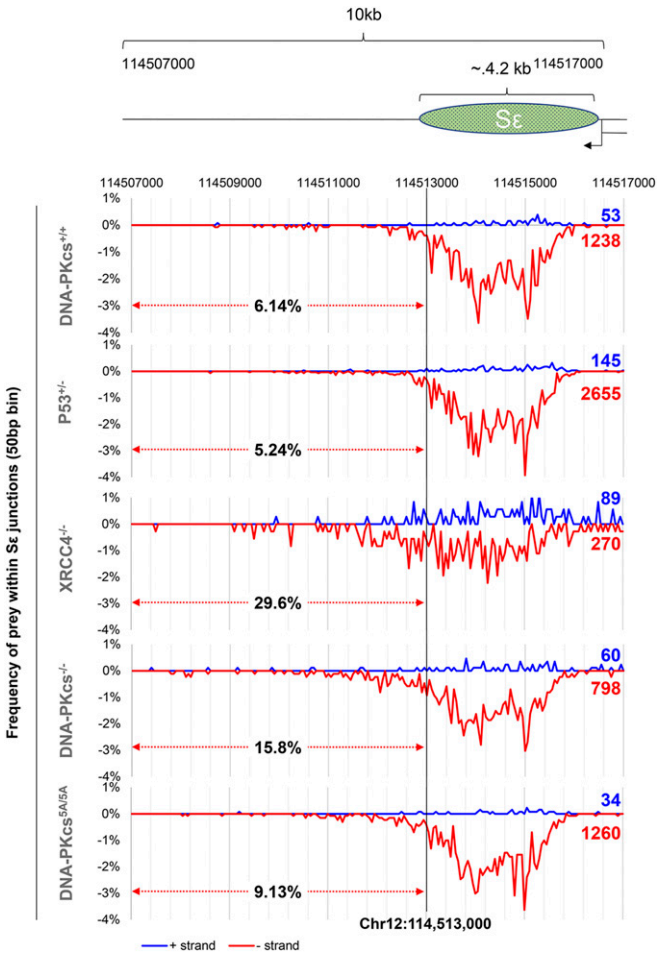

Fig. 5. Distribution of CSR junctions within 10 kb of the Sε locus. The schematic of the region of interest is drawn at *Top*. For each genotype, the number of junctions is indicated for the (+) strand (blue) and (-) strand (red). The (-) orientation junctions are shown as negative percentages. Percent of junctional usage from the end of Sε to the end of the 10-kb window (between chr12:11450700–114513000) is indicated with red arrows (50-bp bin). Junctions in this range are considered resections. Only the percentage of negative strand junctions was used to calculate the resection %. The data represent the pool of five *DNA-PKcs*$^{5A/5A}$ mice, three *DNA-PKcs*$^{+/+}$ mice (WT), two *Xrcc4*$^{-/-}$ mice, five *DNA-PKcs*$^{-/-}$ mice, and a total of four (two each) *Tp53*$^{-/-}$ or *Tp53*$^{+/-}$ mice.

Downloaded at Palestinian Territory, occupied on December 11, 2021
www.manaraa.com

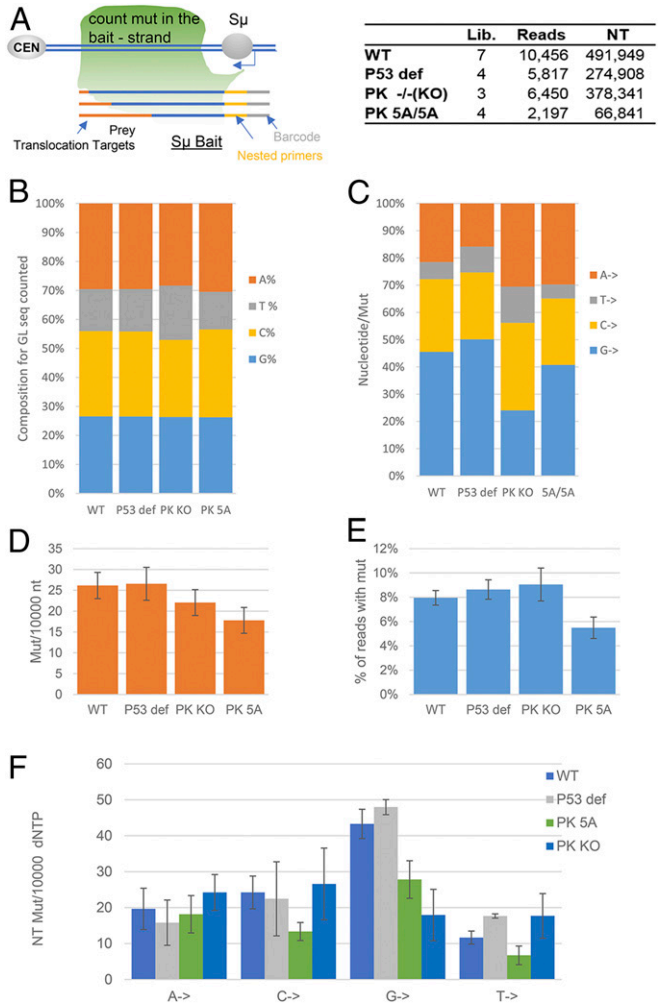

Fig. 6. *DNA-PKcs*$^{5A/5A}$ HTGTS CSR junctions do not have a strong mutational pattern in the IgH region. (*A*) Diagram of the bait site and nucleotide counting scheme for mutational analysis (*Left*). For mutation analyses, we counted the mutations after the nested PCR primer until the end of the bait sequence. There is a clear difference between mutation frequency in IgH junctions vs. non-IgH junctions even if only the bait sequence is compared, so only IgH junctions (both + and - orientation) were counted. The number of independent libraries, reads, and nucleotides analyzed for mutational distribution is shown at *Right*. (*B*) Distribution of nucleotide (A, T, C, or G) frequency in the bait portion used to calculate mutation frequency. (*C*) Frequency of mutations of each nucleotide (A, T, C, or G) in all mutations obtained. (*D*) The overall frequency of mutations per 10,000 nucleotides (nt). (*E*) Frequency of all IgH junctions (reads) containing >0 mutations. (*F*) Mutations in a particular nucleotide per 10,000 of that nucleotide type. The error bars represent SEs. The data represent the collection from four *DNA-PKcs*$^{5A/5A}$ mice, four *DNA-PKcs*$^{+/+}$ mice (WT), four *DNA-PKcs*$^{-/-}$, and two *Tp53*$^{+/-}$ mice.

DNA replication (58, 61) and the relative abundance of sense vs. antisense transcripts (62) could all contribute to this strand bias.

The CSR junctions from *DNA-PKcs*$^{5A/5A}$ and *DNA-PKcs*$^{-/-}$ cells share many features, including end resection and increased MH. T2609 phosphorylation is also dispensable for hairpin opening and V(D)J recombination (22, 35, 37, 38), suggesting a model in which the T2609 cluster phosphorylation promotes end ligation, but is dispensable for end processing and Artemis recruitment. The extent of CSR defects and the increased use of MHs and downstream switch (consistent with end resection) in *DNA-PKcs*$^{5A/5A}$ cells are also consistently less prominent than those from *DNA-PKcs*$^{KD/KD}$ cells, which is comparable to those of *Xrcc4*$^{-/-}$ cells (19, 22). The quantitative nature of the CSR assay and the junctional analyses offered by HTGTS allow us to compare the degree of cNHEJ defects during CSR - *Xrcc4*$^{-/-}$ ≅ *DNA-PKcs*$^{KD/KD}$ >> *DNA-PKcs*$^{-/-}$ > *DNA-PKcs*$^{5A/5A}$ > *DNA-PKcs*$^{PQR/PQR}$ ≅ *DNA-PKcs*$^{+/+}$. Together with the normal CSR in *DNA-PKcs*$^{PQR/PQR}$ B cells with alanine substitutions at the S2056 clusters (34), these results also suggest that another mechanism beyond the loss of DNA-PKcs phosphorylation contributes to the severe cNHEJ defects in *DNA-PKcs*$^{KD/KD}$ cells. The possibilities include other phosphorylation sites (25) or phosphorylation-independent effects of catalysis itself on the structure or organization of the DNA-PKcs protein. Recent structural analyses of DNA-PK holoenzymes have provided evidence for allosteric changes upon DNA-PK activation (63–65), which might link the catalysis directly with DNA-PKcs turnover and its end-protection function.

Increased usage of the Alt-EJ pathway in the residual junctions has been noted in B cells lacking ATM or its downstream factors (50). In this context, although the loss of ATM has been noted in several human cancer cell lines that have adapted to DNA-PKcs inactivation/deletion (66), we and others found that ATM levels or activities are not compromised in DNA-PKcs–deficient primary murine cells or murine models (Fig. 2*D*) (67). Genetic studies in murine models also showed that DNA-PKcs–deficient cells and mice require ATM kinase activity for end ligation and survival (38, 68, 69). Indeed, radiation-induced phosphorylation of ATM substrate—H2AX, Kap1, and Atm itself (S1987) all increased in DNA-PKcs–deficient murine cells (Fig. 2*D*) (67). This could be caused by the accumulation of unrepaired DNA breaks in the absence of DNA-PKcs function. Alternatively, biochemical analyses showed that DNA-PKcs kinase can phosphorylate ATM to suppress ATM kinase activity (67). Since ATM activation is often associated with cell cycle arrest (70, 71), we speculate that ATM inactivation or loss might be selected out DNA-PKcs–deficient human cancer cell lines during the culture to the resulted hyperactivation of ATM. Such adaptation might not be a direct consequence of DNA-PKcs inactivation and, thus, do not have time to accumulate or potentially come with too high a cost (loss of end ligation) in primary murine cells and tissues.

In summary, our findings unequivocally demonstrate an important distinction between autophosphorylation and catalysis on DNA-PKcs, indicating that autophosphorylation at T2609 is largely dispensable for lymphocyte development. Despite the robust CSR efficiency, the CSR junctions recovered from *DNA-PKcs*$^{5A/5A}$ cells reveal a strong bias toward Alt-EJ, suggesting a role of T2609 in promoting cNHEJ at the price of Alt-EJ during CSR.

Data Availability. Sequencing data have been deposited in the Gene Expression Omnibus (GEO) database, https://www.ncbi.nlm.nih.gov/geo/ (accession nos. GSE117628 and GSE54210).

ACKNOWLEDGMENTS. We thank Dr. Wenxia Jiang for her input on the DNA-PKcs KD mouse model. We thank Dr. Chyuan-Sheng (Victor) Lin for technical assistance and advice on the generation of *DNA-PKcs*$^{5A/5A}$ mouse models. We thank other members of the S.Z. laboratory for helpful discussions and technical advice. We apologize to colleagues whose work could not be cited due to space limitations and was covered by reviews instead. This work is in part supported by NIH/National Cancer Institute (NCI) Grants 5R01CA158073, 5R01CA184187, and R01CA226852. S.Z. is the recipient of the Leukemia Lymphoma Society Scholar Award. J.L.C. was supported by NIH/NCI Grants F31CA183504-01A1 and CTSA/NIH TL1 TR000082. This research was funded in part through the NIH/NCI Cancer Center Support Grant P30CA013696 to the Herbert Irving Comprehensive Cancer Center of Columbia University.

Downloaded at Palestinian Territory, occupied on December 11, 2021
www.manaraa.com

1. Y. Ma, U. Pannicke, K. Schwarz, M. R. Lieber, Hairpin opening and overhang processing by an Artemis/DNA-dependent protein kinase complex in nonhomologous end joining and V(D)J recombination. *Cell* **108**, 781–794 (2002).
2. J. Falck, J. Coates, S. P. Jackson, Conserved modes of recruitment of ATM, ATR and DNA-PKcs to sites of DNA damage. *Nature* **434**, 605–611 (2005).
3. K. M. Frank *et al*., Late embryonic lethality and impaired V(D)J recombination in mice lacking DNA ligase IV. *Nature* **396**, 173–177 (1998).
4. Y. Gao *et al*., A targeted DNA-PKcs-null mutation reveals DNA-PK-independent functions for KU in V(D)J recombination. *Immunity* **9**, 367–376 (1998).
5. G. E. Taccioli *et al*., Targeted disruption of the catalytic subunit of the DNA-PK gene in mice confers severe combined immunodeficiency and radiosensitivity. *Immunity* **9**, 355–366 (1998).
6. S. Rooney *et al*., Leaky Scid phenotype associated with defective V(D)J coding end processing in Artemis-deficient mice. *Mol. Cell* **10**, 1379–1390 (2002).
7. P. J. Hung *et al*., MRI is a DNA damage response adaptor during classical non-homologous end joining. *Mol. Cell* **71**, 332–342.e8 (2018).
8. T. Ochi *et al*., DNA repair. PAXX, a paralog of XRCC4 and XLF, interacts with Ku to promote DNA double-strand break repair. *Science* **347**, 185–188 (2015).
9. M. Xing *et al*., Interactome analysis identifies a new paralogue of XRCC4 in non-homologous end joining DNA repair pathway. *Nat. Commun.* **6**, 6233 (2015).
10. V. Kumar, F. W. Alt, R. L. Frock, PAXX and XLF DNA repair factors are functionally redundant in joining DNA breaks in a G1-arrested progenitor B-cell line. *Proc. Natl. Acad. Sci. U.S.A.* **113**, 10619–10624 (2016).
11. X. Liu, Z. Shao, W. Jiang, B. J. Lee, S. Zha, PAXX promotes KU accumulation at DNA breaks and is essential for end-joining in XLF-deficient mice. *Nat. Commun.* **8**, 13816 (2017).
12. M. van der Burg *et al*., A DNA-PKcs mutation in a radiosensitive T-B- SCID patient inhibits Artemis activation and nonhomologous end-joining. *J. Clin. Invest.* **119**, 91–98 (2009).
13. L. Woodbine, A. R. Gennery, P. A. Jeggo, The clinical impact of deficiency in DNA non-homologous end-joining. *DNA Repair (Amst.)* **16**, 84–96 (2014).
14. C. Boboila *et al*., Alternative end-joining catalyzes class switch recombination in the absence of both Ku70 and DNA ligase 4. *J. Exp. Med.* **207**, 417–427 (2010).
15. C. T. Yan *et al*., IgH class switching and translocations use a robust non-classical end-joining pathway. *Nature* **449**, 478–482 (2007).
16. L. Han, K. Yu, Altered kinetics of nonhomologous end joining and class switch recombination in ligase IV-deficient B cells. *J. Exp. Med.* **205**, 2745–2753 (2008).
17. G. C. Bosma *et al*., DNA-dependent protein kinase activity is not required for immunoglobulin class switching. *J. Exp. Med.* **196**, 1483–1495 (2002).
18. J. P. Manis, D. Dudley, L. Kaylor, F. W. Alt, IgH class switch recombination to IgG1 in DNA-PKcs-deficient B cells. *Immunity* **16**, 607–617 (2002).
19. J. L. Crowe *et al*., Kinase-dependent structural role of DNA-PKcs during immunoglobulin class switch recombination. *Proc. Natl. Acad. Sci. U.S.A.* **115**, 8615–8620 (2018).
20. A. Björkman *et al*., DNA-PKcs is involved in ig class switch recombination in human B cells. *J. Immunol.* **195**, 5608–5615 (2015).
21. W. D. Block *et al*., Autophosphorylation-dependent remodeling of the DNA-dependent protein kinase catalytic subunit regulates ligation of DNA ends. *Nucleic Acids Res.* **32**, 4351–4357 (2004).
22. W. Jiang *et al*., Differential phosphorylation of DNA-PKcs regulates the interplay between end-processing and end-ligation during nonhomologous end-joining. *Mol. Cell* **58**, 172–185 (2015).
23. D. W. Chan *et al*., Autophosphorylation of the DNA-dependent protein kinase catalytic subunit is required for rejoining of DNA double-strand breaks. *Genes Dev.* **16**, 2333–2338 (2002).
24. B. P. Chen *et al*., Cell cycle dependence of DNA-dependent protein kinase phosphorylation in response to DNA double strand breaks. *J. Biol. Chem.* **280**, 14709–14715 (2005).
25. P. Douglas *et al*., The DNA-dependent protein kinase catalytic subunit is phosphorylated in vivo on threonine 3950, a highly conserved amino acid in the protein kinase domain. *Mol. Cell. Biol.* **27**, 1581–1591 (2007).
26. D. Merkle *et al*., The DNA-dependent protein kinase interacts with DNA to form a protein-DNA complex that is disrupted by phosphorylation. *Biochemistry* **41**, 12706–12714 (2002).
27. B. P. Chen *et al*., Ataxia telangiectasia mutated (ATM) is essential for DNA-PKcs phosphorylations at the Thr-2609 cluster upon DNA double strand break. *J. Biol. Chem.* **282**, 6582–6587 (2007).
28. P. Douglas *et al*., Identification of in vitro and in vivo phosphorylation sites in the catalytic subunit of the DNA-dependent protein kinase. *Biochem. J.* **368**, 243–251 (2002).
29. H. Yajima, K. J. Lee, B. P. Chen, ATR-dependent phosphorylation of DNA-dependent protein kinase catalytic subunit in response to UV-induced replication stress. *Mol. Cell. Biol.* **26**, 7520–7528 (2006).
30. Q. Ding *et al*., Autophosphorylation of the catalytic subunit of the DNA-dependent protein kinase is required for efficient end processing during DNA double-strand break repair. *Mol. Cell. Biol.* **23**, 5836–5848 (2003).
31. X. Cui *et al*., Autophosphorylation of DNA-dependent protein kinase regulates DNA end processing and may also alter double-strand break repair pathway choice. *Mol. Cell. Biol.* **25**, 10842–10852 (2005).
32. K. Meek, P. Douglas, X. Cui, Q. Ding, S. P. Lees-Miller, trans Autophosphorylation at DNA-dependent protein kinase's two major autophosphorylation site clusters facilitates end processing but not end joining. *Mol. Cell. Biol.* **27**, 3881–3890 (2007).
33. N. Uematsu *et al*., Autophosphorylation of DNA-PKCS regulates its dynamics at DNA double-strand breaks. *J. Cell Biol.* **177**, 219–229 (2007).
34. W. Jiang *et al*., Phosphorylation at S2053 in murine (S2056 in human) DNA-PKcs is dispensable for lymphocyte development and class switch recombination. *J. Immunol.* **203**, 178–187 (2019).
35. S. Zhang *et al*., Congenital bone marrow failure in DNA-PKcs mutant mice associated with deficiencies in DNA repair. *J. Cell Biol.* **193**, 295–305 (2011).
36. S. Zhang *et al*., Spontaneous tumor development in bone marrow-rescued DNA-PKcs(3A/3A) mice due to dysfunction of telomere leading strand deprotection. *Oncogene* **35**, 3909–3918 (2016).
37. Z. Shao *et al*., DNA-PKcs has KU-dependent function in rRNA processing and haematopoiesis. *Nature* **579**, 291–296 (2020).
38. B. S. Lee *et al*., Functional intersection of ATM and DNA-dependent protein kinase catalytic subunit in coding end joining during V(D)J recombination. *Mol. Cell. Biol.* **33**, 3568–3579 (2013).
39. H. Symonds *et al*., p53-dependent apoptosis suppresses tumor growth and progression in vivo. *Cell* **78**, 703–711 (1994).
40. E. Sonoda *et al*., B cell development under the condition of allelic inclusion. *Immunity* **6**, 225–233 (1997).
41. R. Pelanda, S. Schaal, R. M. Torres, K. Rajewsky, A prematurely expressed Ig(kappa) transgene, but not V(kappa)J(kappa) gene segment targeted into the Ig(kappa) locus, can rescue B cell development in lambda5-deficient mice. *Immunity* **5**, 229–239 (1996).
42. Y. Gao *et al*., A critical role for DNA end-joining proteins in both lymphogenesis and neurogenesis. *Cell* **95**, 891–902 (1998).
43. J. Dong *et al*., Orientation-specific joining of AID-initiated DNA breaks promotes antibody class switching. *Nature* **525**, 134–139 (2015).
44. J. Hu *et al*., Detecting DNA double-stranded breaks in mammalian genomes by linear amplification-mediated high-throughput genome-wide translocation sequencing. *Nat. Protoc.* **11**, 853–871 (2016).
45. G. G. Faust, I. M. Hall, YAHA: Fast and flexible long-read alignment with optimal breakpoint detection. *Bioinformatics* **28**, 2417–2424 (2012).
46. S. Franco, F. W. Alt, J. P. Manis, Pathways that suppress programmed DNA breaks from progressing to chromosomal breaks and translocations. *DNA Repair (Amst.)* **5**, 1030–1041 (2006).
47. C. Boboila *et al*., Robust chromosomal DNA repair via alternative end-joining in the absence of X-ray repair cross-complementing protein 1 (XRCC1). *Proc. Natl. Acad. Sci. U.S.A.* **109**, 2473–2478 (2012).
48. S. Franco *et al*., DNA-PKcs and Artemis function in the end-joining phase of immunoglobulin heavy chain class switch recombination. *J. Exp. Med.* **205**, 557–564 (2008).
49. Y. Zhang *et al*., The role of mechanistic factors in promoting chromosomal translocations found in lymphoid and other cancers. *Adv. Immunol.* **106**, 93–133 (2010).
50. R. A. Panchakshari *et al*., DNA double-strand break response factors influence end-joining features of IgH class switch and general translocation junctions. *Proc. Natl. Acad. Sci. U.S.A.* **115**, 762–767 (2018).
51. Y. Zhang *et al*., Spatial organization of the mouse genome and its role in recurrent chromosomal translocations. *Cell* **148**, 908–921 (2012).
52. G. K. Mahowald *et al*., Aberrantly resolved RAG-mediated DNA breaks in Atm-deficient lymphocytes target chromosomal breakpoints in cis. *Proc. Natl. Acad. Sci. U.S.A.* **106**, 18339–18344 (2009).
53. S. Franco *et al*., H2AX prevents DNA breaks from progressing to chromosome breaks and translocations. *Mol. Cell* **21**, 201–214 (2006).
54. R. Wuerffel *et al*., S-S synapsis during class switch recombination is promoted by distantly located transcriptional elements and activation-induced deaminase. *Immunity* **27**, 711–722 (2007).
55. S. Jhunjhunwala, M. C. van Zelm, M. M. Peak, C. Murre, Chromatin architecture and the generation of antigen receptor diversity. *Cell* **138**, 435–448 (2009).
56. A. A. Zarrin, M. Tian, J. Wang, T. Borjeson, F. W. Alt, Influence of switch region length on immunoglobulin class switch recombination. *Proc. Natl. Acad. Sci. U.S.A.* **102**, 2466–2470 (2005).
57. A. A. Zarrin *et al*., An evolutionarily conserved target motif for immunoglobulin class-switch recombination. *Nat. Immunol.* **5**, 1275–1281 (2004).
58. N. J. Haradhvala *et al*., Mutational strand asymmetries in cancer genomes reveal mechanisms of DNA damage and repair. *Cell* **164**, 538–549 (2016).
59. M. S. Neuberger, C. Rada, Somatic hypermutation: Activation-induced deaminase for C/G followed by polymerase eta for A/T. *J. Exp. Med.* **204**, 7–10 (2007).

Downloaded at Palestinian Territory, occupied on December 11, 2021

www.manaraa.com

60. K. Xue, C. Rada, M. S. Neuberger, The in vivo pattern of AID targeting to immunoglobulin switch regions deduced from mutation spectra in msh2-/- ung-/- mice. *J. Exp. Med.* **203**, 2085–2094 (2006).
61. J. I. Hoopes *et al*., APOBEC3A and APOBEC3B preferentially deaminate the lagging strand template during DNA replication. *Cell Rep.* **14**, 1273–1282 (2016).
62. J. Lim *et al*., Nuclear proximity of Mtr4 to RNA exosome restricts DNA mutational asymmetry. *Cell* **169**, 523–537.e15 (2017).
63. X. Yin, M. Liu, Y. Tian, J. Wang, Y. Xu, Cryo-EM structure of human DNA-PK holoenzyme. *Cell Res.* **27**, 1341–1350 (2017).
64. B. L. Sibanda, D. Y. Chirgadze, D. B. Ascher, T. L. Blundell, DNA-PKcs structure suggests an allosteric mechanism modulating DNA double-strand break repair. *Science* **355**, 520–524 (2017).
65. H. Sharif *et al*., Cryo-EM structure of the DNA-PK holoenzyme. *Proc. Natl. Acad. Sci. U.S.A.* **114**, 7367–7372 (2017).
66. J. A. Neal, K. Meek, Deciphering phenotypic variance in different models of DNA-PKcs deficiency. *DNA Repair (Amst.)* **73**, 7–16 (2019).
67. Y. Zhou *et al*., Regulation of the DNA damage response by DNA-PKcs inhibitory phosphorylation of ATM. *Mol. Cell* **65**, 91–104 (2017).
68. S. Zha *et al*., Ataxia telangiectasia-mutated protein and DNA-dependent protein kinase have complementary V(D)J recombination functions. *Proc. Natl. Acad. Sci. U.S.A.* **108**, 2028–2033 (2011).
69. E. Callén *et al*., Essential role for DNA-PKcs in DNA double-strand break repair and apoptosis in ATM-deficient lymphocytes. *Mol. Cell* **34**, 285–297 (2009).
70. D. Menolfi, S. Zha, ATM, ATR and DNA-PKcs kinases-the lessons from the mouse models: Inhibition ≠ deletion. *Cell Biosci.* **10**, 8 (2020).
71. Y. Shiloh, ATM: Expanding roles as a chief guardian of genome stability. *Exp. Cell Res.* **329**, 154–161 (2014).

Downloaded at Palestinian Territory, occupied on December 11, 2021

www.manaraa.com